Diagnosing Ozone-NO$_x$-VOCs-Aerosols Sensitivity and Uncovering Causes of Urban-Nonurban Discrepancies in Shandong, China using Transformer-Based Estimations

Chenliang Tao[1], Yanbo Peng[1,2,*], Qingzhu Zhang[1,*], Yuqiang Zhang[1], Bing Gong[3], Qiao Wang[1], Wenxing Wang[1]

[1]Big Data Research Center for Ecology and Environment, Environmental Research Institute, Shandong University, Qingdao 266237, P.R. China

[2]Shandong Academy for Environmental Planning, Jinan 250101, P.R. China

[3]Jülich Supercomputing Centre, Forschungszentrum Jülich, 52425 Jülich, Germany

Keywords:

Air pollution, Deep learning, Transformer, Satellite, Urban-rural difference, Ozone Regime

____

*Corresponding authors. E-mail: zqz@sdu.edu.cn, pengyanbo@mail.sdu.edu.cn

Abstract

Narrowing surface ozone disparities between urban and nonurban areas escalate health risks in densely populated urban zones. A comprehensive understanding of the impact of ozone photochemistry on this transition remains constrained by current knowledge of aerosol effects and the availability of surface monitoring. Here we reconstructed spatiotemporal gapless air quality concentrations using a novel Transformer deep learning (DL) framework capable of perceiving spatiotemporal dynamics to analyze ozone urban-nonurban differences. Subsequently, the photochemical effect on these discrepancies was analyzed by elucidating shifts in ozone regimes inferred from an interpretable machine learning method. The evaluations of model exhibited an average out-of-sample cross-validation coefficient of determination of 0.96, 0.92, and 0.95 for ozone, nitrogen dioxide, and fine particulate matter ($PM_{2.5}$), respectively. The ozone sensitivity in nonurban areas, dominated by nitrogen oxide (NO_x)-limited regime, was observed to shift towards increased sensitivity to volatile organic compounds (VOCs) when extended to urban areas. A third 'aerosol-inhibited' regime was identified in the Jiaodong Peninsula, where the uptake of hydroperoxyl radicals onto aerosols suppressed ozone production under low NO_x levels during summertime. The reduction of $PM_{2.5}$ would increase the sensitivity of ozone to VOCs, necessitating more stringent VOC emissions abatement for urban ozone mitigation. In 2020, urban ozone levels in Shandong surpassed those in nonurban areas, primarily due to a more pronounced decrease in the latter resulting from stronger aerosol suppression effects and lesser $PM_{2.5}$ reductions. This case study demonstrates the critical need for advanced spatially resolved models and interpretable analysis in tackling ozone pollution challenges.

1. INTRODUCTION

Surface ozone (O_3), fine particulate matter ($PM_{2.5}$), and nitrogen dioxide (NO_2) are among the most important trace gases in the atmosphere that significantly impact the ecological environment and public health (Han and Naeher, 2006; Yue et al., 2017). During the Action Plan on the Prevention and Control of Air Pollution (denoted as the Clean Air Action, 2013-2017) (Action Plan on Air Pollution Prevention and Control (in Chinese), 2023), $PM_{2.5}$ and nitrogen oxide (NO_x = nitric oxide (NO) + NO_2) emissions across China decreased by 33% and 21%, respectively (Zheng et al., 2018), while surface O_3 exhibited an increasing trend (Lu et al., 2018). The increase in O_3 could be partially attributed to the "aerosol-inhibited" effect, where the reduction in $PM_{2.5}$ results in a diminished reactive uptake of hydroperoxyl radicals (HO_2) onto aerosols (Ivatt et al., 2022; Li et al., 2019). The societal benefits of reducing premature deaths and economic losses from $PM_{2.5}$ reductions have been diminished by the rising O_3 (Liu et al., 2022). Thus, achieving the joint attainment objectives for $PM_{2.5}$ and O_3 has been put on the top priority of China's long-term air pollution control policies.

The complexity of the O_3 formation is partly reflected by the nonlinear response to changes in precursors (i.e. volatile organic compounds (VOCs) and NO_x), as well as the presence of heterogeneous reactions in aerosols. Understanding these dynamics is crucial to investigate current narrowing differences in O_3 concentrations between urban and nonurban areas, which have traditionally shown higher levels in rural (Han et al., 2023). The formaldehyde-to-NO_2 ratio (HCHO/NO_2 or FNR) serves as a theoretical

66 gauge of the relative abundance of total organic reactivity to hydroxyl radicals (OH)

67 and NO_x (Wei et al., 2022c; Sillman, 1995), and as such, it can function as a useful

68 indicator of O_3 sensitivity. Previous studies have utilized the $HCHO/NO_2$ from satellite

69 remote sensing to infer O_3 production regimes for guiding O_3 control policies (Jin et al.,

70 2023; Li et al., 2021a; Jin et al., 2020). However, the changes of $HCHO/NO_2$ threshold

71 in O_3 regimes classification modulated by meteorology and localized atmospheric

72 chemistry in space and time, and uncertainties relating column to surface, precluding

73 robust applications over larger spatial scales (Lee et al., 2023; Jin et al., 2017; Souri et

74 al., 2023). While the observation-based model method alleviates some of these

75 limitations, constraints remain including computational demands and priori chemical

76 mechanisms (Song et al., 2022b; Chu et al., 2023). The advent of interpretable machine

77 learning models affords new opportunities to unravel intricate dependencies governing

78 O_3 formation purely from actual observational data. However, sparse ground-based

79 monitoring stations, especially in rural areas, pose great challenges to the spatially full

80 coverage of studies. Thus, the high-spatiotemporal-resolutions estimations of surface

81 air pollutants are urgently needed to improve our understanding of how these pollutants

82 are changing and interacting.

83   Recent studies have utilized spatially resolved remote sensing data to estimate the

84 continuous distribution of air pollutants in space by diverse machine learning (ML)

85 models (Lyapustin and Wang, 2022; Lamsal et al., 2022; Huang et al., 2021; Li and

86 Wu, 2021; Ren et al., 2022b), such as random forest (RF), full residual deep learning,

87 and Bayesian ensemble model. These attempts have demonstrated the tremendous

88 potential of machine learning as an alternative to atmospheric chemical models (Jung

89 et al., 2022). Nevertheless, there are still several aspects that have not been fully

90 considered. For instance, coarse-resolution maps limit the ability to characterize the

91 fine-scale variation of air pollution within urban areas, which has significant

92 implications for environmental justice disparities of disadvantaged communities

93 (Jerrett et al., 2005; Ren et al., 2022b; Dias and Tchepel, 2018). Additionally, existing

94 ML models may not fully account for the complex atmospheric chemistry and physics

95 processes that influence pollutant concentrations due to the single-pixel-based

96 processing mode (Huang et al., 2021; Requia et al., 2020; Thongthammachart et al.,

97 2022; Li et al., 2022b; Geng et al., 2021). Although several efforts have been made by

98 using the neural network with convolutional layers (Di et al., 2016), and explicitly

99 incorporating spatiotemporally weighted information to machine learning models (Wei

100 et al., 2022b), the global spatiotemporal self-correlation of multi-dimensional features

101 in the input array remained unaddressed. Meanwhile, the convolutional operations

102 extract features from all neighboring grids of the target, ignoring the fact that the

103 environmental knowledge of the target grid itself is the most significant, with the

104 adjacent features being secondary.

105   In this study, we aim to analyze the evolving dynamics of urban-nonurban O_3

106 differences between 2019 and 2020. The roles of emission discrepancies and

107 nonlinearity of O_3-NO_x-VOCs-aerosols photochemical processes in shaping these O_3

108   variations were deeply dissected. To achieve a comprehensive analysis, we employed a

109   new spatiotemporal Transformer framework that paid special attention to air mass

110   transport and dispersion affected by the spatial-temporal correlations, to reconstruct the

111   spatially gapless air quality datasets based on satellite data, ground-level observations,

112   and meteorological reanalysis. The estimations are particularly vital for regions lacking

113   dense ground-based monitors, ensuring that our understanding of O_3 dynamics in urban-

114   nonurban areas and formation regimes is not limited by geographical constraints in data

115   availability. Surface O_3 formation regimes in Shandong province were inferred by the

116   classic XGBoost model (Chen and Guestrin, 2016) coupled with Shapley Additive

117   exPlanations (SHAP) (Lundberg and Lee, 2017), which identifies the impact of

118   meteorological conditions and photochemical indicators (i.e. $PM_{2.5}$ as a proxy for

119   aerosols, NO_2 as a proxy for NO_x, and HCHO as a proxy for VOCs) on O_3. The

120   innovative Transformer-based modeling and interpretable machine learning analysis

121   approaches are expected to enable new applications such as those of air quality

122   simulation and O_3 formation regimes studies.

123   **2. MATERIALS AND METHODS**

124   **2.1 Predictor Variables**

125   The study domain covered the Shandong province of China, which has a high

126   mortality burden of air pollution (Liu et al., 2017). The surface $PM_{2.5}$, O_3, and NO_2

127   concentration measurements were collected from the regulatory air quality stations of

128   the China National Environmental Monitoring Center (CNEMC, with a total of 179

129   locations) and the Shandong Provincial Eco-environmental Monitoring Center (SDEM,

130   with a total of 166 locations) (Figure S1). The SDEM stations were included to fill the

131   spatial gaps in the county and rural areas where CNEMC stations were lacking. The

132   study area was divided into 1.22 million grid cells with a spatial resolution of 500

133   meters. We utilized a range of predictor data, including tropospheric NO_2 vertical

134   column densities (VCDs) and O_3 total VCDs measured by TROPOspheric Monitoring

135   Instrument (TROPOMI) (Lamsal et al., 2022; Copernicus Sentinel-5P (processed by

136   ESA), 2020), aerosol optical depth (AOD) data and atmospheric properties obtained

137   from Moderate Resolution Imaging Spectroradiometer (MODIS) Multi-Angle

138   Implementation of Atmospheric Correction products (Lyapustin and Wang, 2022),

139   AOD estimates from Modern-Era Retrospective Analysis for Research and

140   Applications as the supplement to MODIS (2015), meteorological reanalysis obtained

141   from the fifth generation atmospheric reanalysis dataset of European Centre for

142   Medium-Range Weather Forecasts (ECMWF) (ERA5) (Hersbach et al., 2023, p.5),

143   daily dynamic industrial emissions, moonlight-adjusted nighttime lights product

144   (Román et al., 2018), vegetation index (Didan, 2021), population density (WorldPop,

145   2018), road density, land use data (Jun et al., 2014), and the shuttle radar topography

146   mission digital elevation model. The detailed information for all predictive variables

147   is listed in Table S1 and discussed in Text S1-2. Taking space-variant and seasonal

148   patterns into consideration, several spatiotemporal indicators such as geographical

149   coordinates, Euclidean spherical coordinates, year, Julian date, and helix-shaped

150 trigonometric sequences, were also included as predictor variables (Text S3) (Sun et al.,

151 2022). Geographic Information Systems techniques, including reprojection and

152 resampling, were used to consolidate all the data obtained for consistent projection and

153 spatial scale. Finally, the Light Gradient Boosting Machine was used to fill satellite data

154 gaps (Text S4) (Ke et al., 2017).

155 **2.2 Air Transformer**

156 AiT is an individual Transformer model that adopts an encoder-decoder

157 architecture with multidimensional self-attention computation to dynamically capture

158 the spatiotemporal autocorrelation of atmospheric pollution changes from the

159 sequences of pixels and variables for more reliable spatial maps of estimation.

160 Compared with existing image and video recognition Transformers, such as ViT

161 (Dosovitskiy et al., 2021), Timesformer (Bertasius et al., 2021), and Uniformer (Li et

162 al., 2021b), AiT is innovative in incorporating self-attention across channels after the

163 pixels-based self-attention and taking advantage of the decoder. The former can capture

164 the correlations between predictor variables. The decoder was employed to enable

165 interaction between the primary target grid and neighboring grids. Predictor variables

166 with 8 timesteps within 1000 meters of the target grid cell were fed into the model to

167 learn spatiotemporally disparities among atmospheric pollutants for predicting O_3, NO_2

168 and $PM_{2.5}$ within the target grid point.

169 The overall architecture of the proposed AiT model and the dimensions of input

170 data are illustrated in **Figure 1**. The encoder maps an input sequence with neighborhood

171   spatiotemporal data to a sequence with high-dimensional spatiotemporal characteristics,

172   and the decoder generates an estimation by computing self-attention representations

173   between the target grid and outputs of the encoder. The encoder of AiT takes as input a

174   clip $X \in R^{V \times T \times H \times W}$ consisting of T multi-variable frames of size $H \times W$ sampled

175   from the original dataset, where V is the number of variables and the target grid cell is

176   located at ($\left\lceil \frac{H}{2} \right\rceil$, $\left\lceil \frac{W}{2} \right\rceil$). The decoder takes as input a clip $X \in R^{V \times 1 \times 1 \times 1}$ consisting of V

177   variables from the target grid. Several Transformer blocks with modified self-attention

178   computation (AiT blocks) are applied to the encoder. The AiT encoder block is similar

179   to the standard vision transformer block but specifically designed for atmospheric

180   estimation (Dosovitskiy et al., 2021). It is a stack of two self-attention schemes,

181   including global spatiotemporal self-attention on the pixels and channel self-attention

182   on variable predictors. The former contains $N = HW$ effective input sequence length

183   for the self-attention to extract spatiotemporal information. The latter computes self-

184   attention based on V effective input sequence length to capture hidden information on

185   variables. The decoder part is symmetric to the encoder part, but it only has a block

186   with the spatiotemporal self-attention mechanism. We compute the matrix of self-

187   attention outputs as:

188
$$Attention(Q, K, V) = \text{softmax}\left(\frac{QK^T}{\sqrt{d_k}} + B \right) V \qquad (1)$$

189   where Q, K, and V are the queries, keys, and values in the inputs of the particular

190   attention, respectively. d_k is the feature dimensionality of K, and B is the geographic

191   positional bias term. Another difference is that the attention function of the decoder is

192 computed on Q from the estimated grid data, and (K, V) from the outputs of encoder

193 blocks under the same stage, resulting in the outputs of the last decoder block being

194 sized 1 × 128. The description of the data transformation and design details in the

195 process of training can be found in Text S5. The multi-task learning strategy was also

196 applied for learning representation across multiple pollutant estimation tasks (Text S6).

197 The aggregated feature data from June 2019 to June 2021 were utilized to train and

198 validate the model through cross-validation (CV), where the optimal model, trained

199 based on out-of-sample CV, was used to estimate multiple pollutant concentrations

200 during the study period, which was then employed for subsequent analysis.
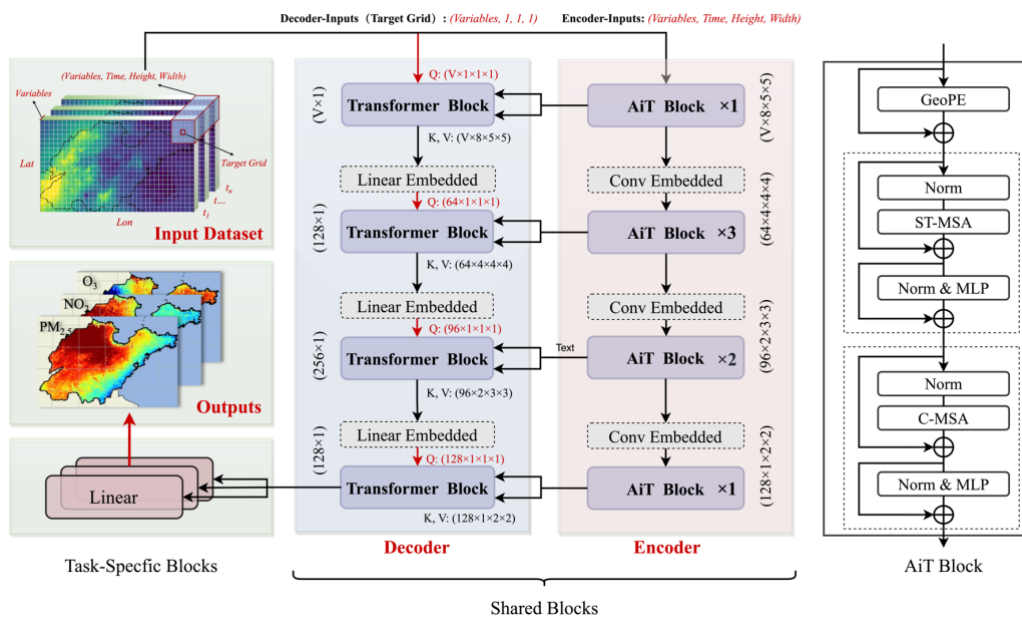
201

202 **Figure 1.** Schematic diagram of the AiT model. The white box of multi-dimension
203 inputs presents each pixel of raster data. The AiT Block is a Transformer block based
204 on self-attention across space, time, and variables. The GeoPE, Norm, MLP, ST-MSA
205 and C-MSA indicate respectively positional embedding, layer normalization, multi-
206 layer perceptron, spatial-temporal multi-head self-attention and multi-channels (multi-
207 variables) multi-head self-attention.

2.3 Diagnosing O_3 Formation Sensitivity

Interpretability can provide insight into how a model may be improved, bolster the understanding of the process being modeled, and engender appropriate confidence among researchers. SHAP is a coalitional game-theoretic approach based on Shapley values (Shapley, 1988) and then assigns each variable an importance value for a particular estimation. Deep SHAP, a high-speed approximation algorithm that builds on the connection between Shapely values and DeepLIFT (Shrikumar et al., 2019), is employed to compute the feature importance of AiT from all data with monitoring labels for interpreting the prediction. The sensitivity of the O_3 formation regime was deduced using a combination of the XGBoost model and SHAP interpretability method, employing the GPUTreeShap algorithm (Mitchell et al., 2020), which simulated the response of surface O_3 to meteorological conditions, HCHO, NO_2 and $PM_{2.5}$, by utilizing the continuous estimations from ERA5, AiT and TROPOMI between 2019 and 2020. The incorporation of meteorology in the model ameliorated the inadequacies in the conventional method (HCHO-NO_2 ratio), where its thresholds for identifying O_3 regimes vary temporally and spatially. The positive or negative contributions of three atmospheric pollutants were used to identify their promoting or inhibitory effects on O_3 variability. Given the unbiased property of SHAP values regarding directionality, the normalized relative magnitudes of SHAP values were calculated for HCHO, NO_2, and $PM_{2.5}$. This allowed the differentiation of the O_3 formation regimes based on the locally maximal proportions of the SHAP values for each species. The ground-level monthly

229 HCHO concentrations were derived using a combination of column-to-surface

230 conversion factor (CF) simulated from the ECMWF Atmospheric Composition

231 Reanalysis 4 and the tropospheric HCHO VCDs obtained from TROPOMI (Cooper et

232 al., 2022; Su et al., 2022; Inness et al., 2019). A detailed description of the CF method

233 as used here is discussed in Text S7. To ensure consistency in resolution between

234 TROPOMI and AiT, we employed the oversampling method to downscale the

235 TROPOMI VCDs to the resolution of AiT estimation, which has been proven effective

236 in achieving finer resolution (Su et al., 2022; Cooper et al., 2022; van Donkelaar et al.,

237 2015).

238 **3. RESULTS AND DISCUSSION**

239 **3.1 Performance Evaluation for the AiT**

240 **3.1.1 Cross-validation Metrics**

241 We evaluated the AiT performance using the 10-fold CV approach (Text S8), with

242 correlation coefficient (R^2) measuring the extent to which model simulations explain

243 variability in atmospheric pollutants, and root mean square errors (RMSE) and mean

244 absolute errors (MAE) evaluating the bias/error of the estimates. As shown in **Figure**

245 **2**, out-of-sample CV daily ground-level O_3, NO_2, and $PM_{2.5}$ estimations are highly

246 consistent with ground observations ($R^2 = 0.96, 0.92, 0.95$), indicating low uncertainties,

247 with RMSE of 10.1, 4.7, and 8.5 $\mu g/m^3$ and MAE of 7.2, 3.5, and 5.3 $\mu g/m^3$ for the

248 2018-2021 period. The linear regression comparing the O_3 predictions versus

249 observations yields a slope of 0.98 and an intercept of 2.39, which demonstrates that

250   there is no systematic bias in the estimations. Meanwhile, as shown in Figure S3, our

251   AiT model performs well at the individual-site scale with high CV-RMSE for O_3, NO_2,

252   and $PM_{2.5}$ (10.5 ± 8.6, 4.7 ± 1.1, and 8.3 ± 2.8 µg/m³). In general, the AiT model is

253   robust for multi-pollutant simultaneous estimations.
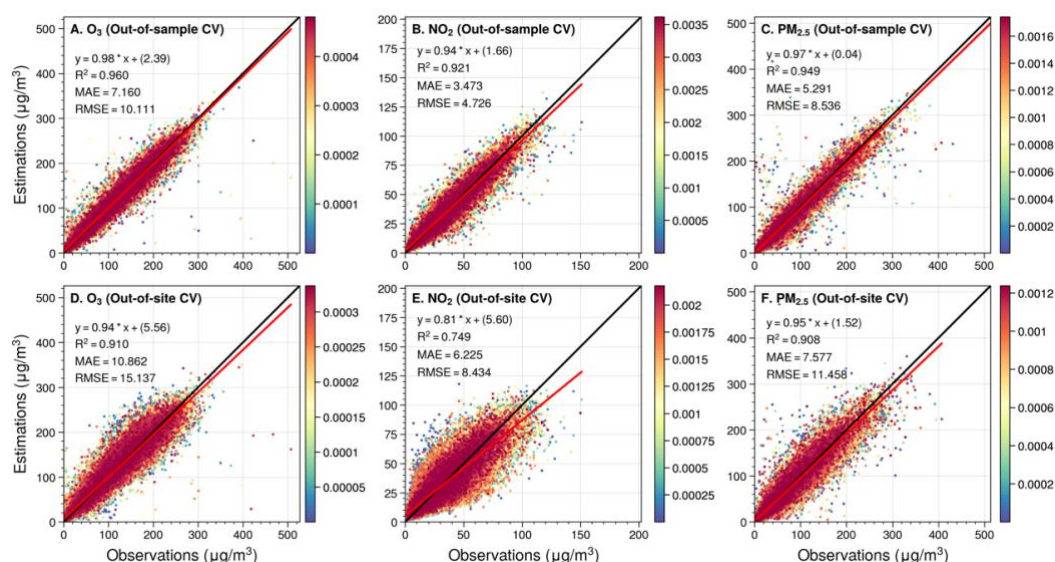
255   **Figure 2.** Out-of-sample cross-validation (A-C) and out-of-site cross-validation (D-F)

256   of daily ground-level O_3, NO_2 and $PM_{2.5}$ concentration in the validation set.

257   The spatial generalization ability of the AiT is then examined by the out-of-site CV

258   evaluation method (**Figure 2**). The daily spatial variations of O_3, NO_2, and $PM_{2.5}$ at

259   locations without ground measurements can be well estimated by our model (i.e., CV-

260   R^2 = 0.91, 0.75, 0.91), representing a core contribution of such studies. We also probe

261   the model performance for each site separately based on spatial CV estimations (Figure

262   S4). This general model yields an RMSE of 15.2 ± 8.8, 8.1 ± 2.7, and 11.1 ± 2.8 µg/m³,

263   respectively. Furthermore, we trained the AiT model using data exclusively from

264   CNEMC and assessed its generalizability by validating it with data from SDEM. The

265   model demonstrates strong performance with high our-of-sample CV R^2 values in the

266   validation dataset of CNEMC (Figure S5), and when evaluated with SDEM data, it

267   exhibits only an acceptable degradation in predictive accuracy (Figure S6, R^2 for O_3,

268   NO_2, and $PM_{2.5}$: 0.90, 0.73, 0.79). Meanwhile, our framework utilizes multi-task

269   learning to enhance computational efficiency through a single iteration and leverages

270   the interactions among multiple pollutants to optimize the performance at individual

271   pollutant levels (Table S2). In summary, AiT provides relatively stable estimations in

272   areas without available ground-level monitoring and reliably extends ground

273   monitoring from the site scale to the full-coverage spatial scale with high spatial

274   resolution.

275   **3.1.2 Compared with Other ML Models**

276   Since ground-level air quality measurements across the target regions are

277   extremely limited at a 500 m spatial resolution, representing only roughly two-

278   thousandths of the total grid cells, we seek implicit approaches to validate our estimated

279   near surface pollutant concentrations. We compared the model performance with

280   previous studies that applied different ML methods to estimate these three air pollutants

281   individually and found out that our cross-validation results are comparable or even

282   better than those (Table S3). We also created a new dataset in our study by applying the

283   classic RF algorithm which is the most common ML model for estimating atmospheric

284   pollution in recent years (Wei et al., 2022a; Requia et al., 2020; Xiao et al., 2018; Geng

285   et al., 2021; Lu et al., 2021) with the same variables as AiT. The statistical comparisons

286   between AiT and RF are also shown in Table S3. We then compared the spatial

287   distribution of our results with estimations from CHAP, AiT-CNEMC, and RF.

288   **Figure 3** shows the spatial maps of near-surface air pollutants with partially

289   zoomed satellite images for monitoring sites, AiT, CNEMC-trained AiT, RF, and CHAP

290   in 2019 (see Figure S7 for 2020). We found that the estimated NO_2 and $PM_{2.5}$ from the

291   AiT share a similar spatial distribution to those estimated by RF and CHAP. However,

292   enlarged city-level urban regions in **Figure 3** reveal that AiT estimates fine structures

293   and intra-urban disparities in near-surface multi-pollutant concentrations, which cannot

294   be captured by either RF or CHAP products. This spatial gradient is also captured by

295   AiT trained with CNEMC data, revealing the reliability of the deep learning model

296   structure. In general, while RF and CHAP can only identify the hotspots of air pollutants

297   at a regional scale, the spatial distribution of air pollutants estimated by AiT shows

298   much more detailed differences with high spatial and temporal variability across the

299   city scale. The differences of near-surface annual averaged pollutants between 2019 and

300   2020 for measured and multi-estimated data are presented in Figure S8. The reductions

301   or increases of O_3, NO_2, and $PM_{2.5}$ in distinct locations can be simulated by our model,

302   which is relatively consistent with the changes of measurements. The zoomed maps in

303   Figure S7 show the differences in three pollutant concentrations at the city scale of the

304   capital of Shandong Province, Jinan. It can be found that the change in pollutant levels

305   in 2020 compared to 2019 exhibits substantial regional variations and intra-urban

306   heterogeneity, with some areas experiencing an increase while others a decrease.

307   Compared to the estimations of RF and CHAP, our results successfully capture the

complex distribution of air pollution in reality and reveal that the decline in PM$_{2.5}$ is

primarily concentrated in suburban areas, while an increase is pronounced in some

regions of urban during 2020. Notably, this spatial trend may be consistent with

underlying emission patterns and meteorological conditions.
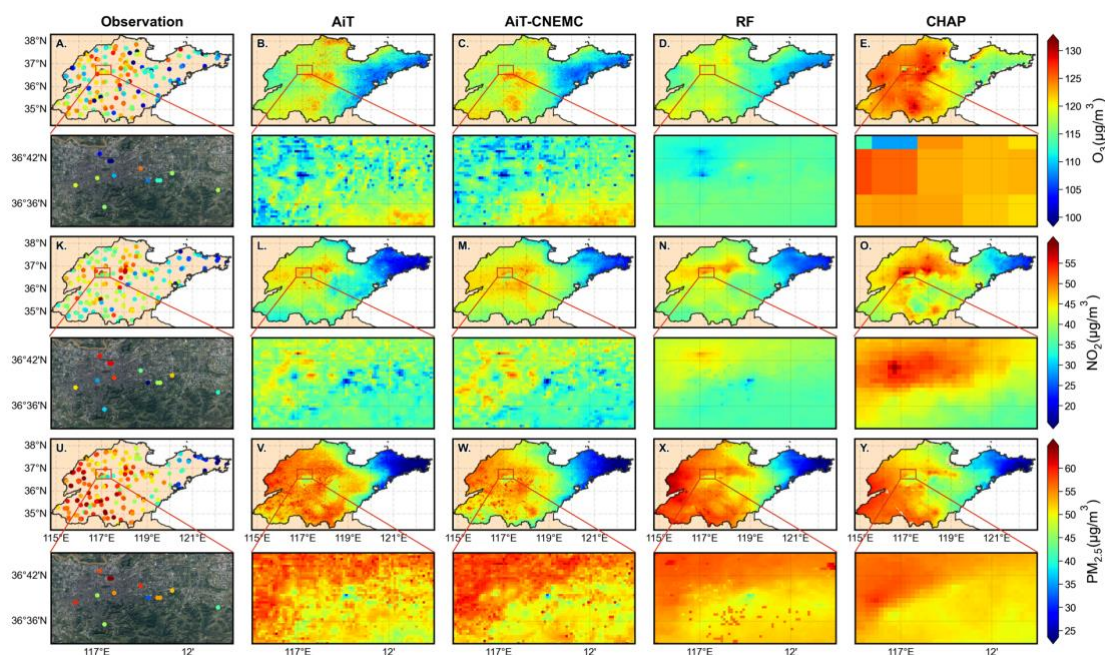
Figure 3. Spatial distribution of the annual mean (A-E) O$_3$, (K-O) NO$_2$, and (U-Y)

PM$_{2.5}$ concentrations from observations, Air Transformer (AiT), CNEMC-trained AiT,

Random Forest (RF) and ChinaHighAirPollutants (CHAP), respectively, in 2019. The

region enclosed by the red rectangular box corresponds to the zoomed-in maps of the

satellite (© Tianditu: www.tianditu.gov.cn) and pollutant concentrations at a city scale

for the capital city of Shandong Province, Jinan.

3.1.3 Typical Event Study

The typical example of the spatial distribution of multi-pollutant observations and

estimations of AiT is compared for validating the predictive capability of the model at

a particular pollution episode, i.e., 13-16 March 2021. During this period, an early

season dust storm, which was called the largest and strongest such storm in a decade,

324 hits northern China (Myers, 2021). As shown in **Figure 4**, our model can capture the

325 spatial distribution of surface O_3, NO_2, and $PM_{2.5}$ in the time of severe atmospheric

326 pollution. In addition, our estimations are in high concordance with measurements in

327 terms of magnitudes and spatial variability over the entire research region. The model

328 trained solely on CNEMC data is also capable of effectively capturing the drastic

329 changes in air quality during the pollution episode (Figure S9). Combining wind fields

330 to analyze $PM_{2.5}$ distribution on the day of the dust storm, it can be found that surface

331 wind carries a massive amount of particulate matter from Beijing, which suffered a

332 severe dust storm, to northern Shandong. The influence was gradually diminishing in

333 southern Shandong due to the obstruction of Mount Tai. Spatial heterogeneity within

334 intra-urban areas was further investigated to identify the hotspots of pollution sources.

335 The satellite images in even-numbered rows of **Figure 4** illustrate the spatial disparities

336 of three pollutants around four typical emission sources: thermal power plants,

337 industrial parks, overpasses, and parks. As depicted, these anthropogenic emission

338 sources contribute to higher pollution levels, while the mountain in the park mitigates

339 primary pollution but also increases O_3 concentrations. Industrial sources emit a large

340 number of NO_x and $PM_{2.5}$, leading to increased pollution of these species compared

341 with other urban microenvironments, which in turn promotes O_3 formation, particularly

342 in downwind areas (Miller et al., 1978; Tang et al., 2020). Although the spatial gradients

343 of pollutants on the street are not as apparent as in the dataset with 100 m resolution

344 (Huang et al., 2021), the predicted spatial variation between various geographical

345 scenes is in satisfactory agreement given the 500 m scale of the model. Urban areas

346 affected by diverse dust pollution exhibit lower $PM_{2.5}$ concentrations compared to rural

347 due to the obstructive and filtering effects of artificial structures, such as buildings and

348 urban greenery (Figure S10), which cannot be effectively captured solely by ground-

349 based observations. Notably, the elevated $PM_{2.5}$ inhibits the formation of O_3 by

350 diminishing solar radiation flux and absorbing the HO_2 radical on the aerosol surface,

351 even in conditions characterized by similar NO_2 levels. As for the mapping, AiT

352 accurately grasps the spatial characteristics of air pollutants and delivers a coherent

353 spatial-temporal distribution that is consistent with the prior knowledge of atmospheric

354 transport.
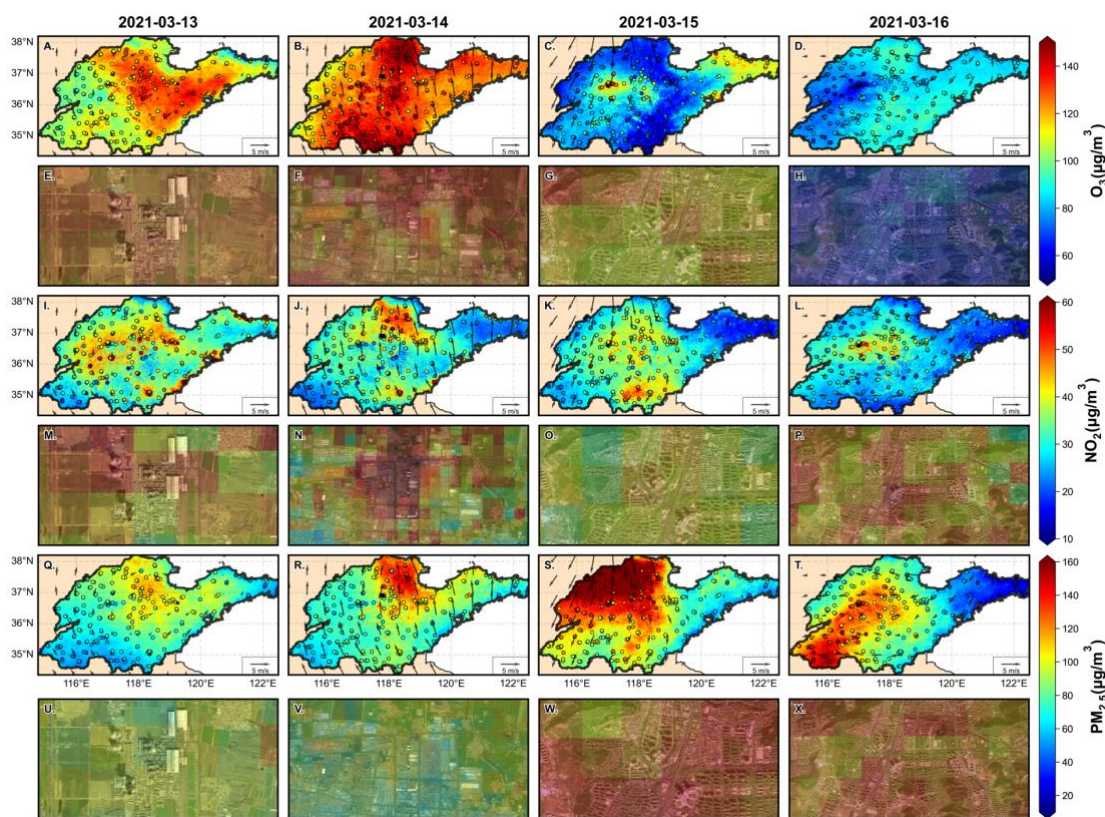
355

356 **Figure 4.** The spatial distribution of ground-level O_3 (A-D), NO_2 (I-L), and $PM_{2.5}$ (Q-
357 T) concentrations from AiT and monitoring stations during 13-16 March 2021 in

358 Shandong, China. The black arrows are the 10 m wind speed and wind direction. The
359 even-numbered rows correspond to the concentration distribution maps of typical
360 emission sources for the respective pollutants, accompanied by satellite images (©
361 Tianditu: www.tianditu.gov.cn). The upper right area of E, M, and U is a thermal power
362 plant in Weifang City (119°250′E-119°280′E, 36°658′N-36°673′N). The center area of
363 F, N, and V is an industrial park in Zibo city (117°725′E-117°845′E, 36°880′N-
364 36°940′N). The center and upper right area of G, O, and W is an overpass and Wanling
365 mountain in Jinan city (116°977′E-117°009′E, 36°590′N-36°606′N). The center area of
366 H, P, and X is another overpass in Jinan city (116°970′E-117°030′E, 36°580′N-
367 36°610′N).

368 **3.2 Urban-nonurban Difference**

369 Full-coverage pollutant estimates provide a foundational basis for assessing urban-

370 nonurban disparities, addressing the critical issue of imbalanced site numbers between

371 urban and rural locations. Table S4 shows the concentrations of O_3, NO_2, $PM_{2.5}$, and

372 HCHO over the urban and nonurban regions, delineated from an annual urban extent

373 dataset (Zhao et al., 2022). The urban extents in Shandong Province in 2019 are

374 depicted in Figure S11. From 2019 to 2020, surface air pollutant levels declined

375 significantly in Shandong. The averaged concentration discrepancies of these pollutants

376 between urban and nonurban over February to March (lockdown during COVID-19)

377 and June to October (summertime) are shown in **Figure 5**. Surface concentrations of

378 NO_2 and HCHO are higher in urban than nonurban areas, and the differences narrowed

379 from February to October, while $PM_{2.5}$ is the opposite at both. Ground-level O_3 levels

380 exhibited unexpected urban-nonurban disparity variations, from the lockdown period

381 through the summer, as well as from 2019 to 2020. Compared to nonurban areas, the

382 urban areas, which previously had lower O_3 levels, began to experience higher

383 concentrations, attributed to a more rapid decline of ozone in nonurban regions. **Figure**

384 **6** revealed that urban-nonurban differences in O_3 and $PM_{2.5}$ varied across various cities

385 during the lockdown period in 2019, while the higher NO_2 pollution in urban areas

386 remained consistent. In summer, only a handful of urban areas exhibit lower levels of

387 ozone concentration, where NO_2 and $PM_{2.5}$ levels surpass those in nonurban regions,

388 attributable to a more pronounced titration effect of NO and a slower rate of

389 photochemistry reactions (Figure S12) (Sicard et al., 2016, 2020; Zhang et al., 2004).

390 Comparative urban-nonurban differences from 2019 to 2020 indicate an accelerated

391 reduction of ozone and HCHO in non-urban areas, while NO_2 and $PM_{2.5}$ levels in urban

392 have seen a more significant decrease due to the decline in anthropogenic activities,

393 particularly the suspension of emissions from pollution sources located in urban areas.

394 Upon comparing the results of urban-nonurban disparities of our data with monitoring

395 data and the CHAP dataset, we have identified potential overestimations or

396 underestimations across various cities in monitoring data, likely resulting from the

397 limited number of non-urban sites (**Figure 6**P, S13). The notable disparity between the

398 number of urban and non-urban sites in cities such as JNA, LC, LY, QD, and YT results

399 in a pattern of urban-nonurban differences that contrasts markedly with the observed in

400 AiT (Table S5). The urban-nonurban difference calculated by the CHAP generally

401 aligns with our findings (Figure S14). Nevertheless, it is worth noting that the coarse

402 resolution of O_3 (10 km) has led to a significant overestimation. These results highlight

403 the invaluable of high-resolution and gapless data for studying urban-nonurban

404   disparities.
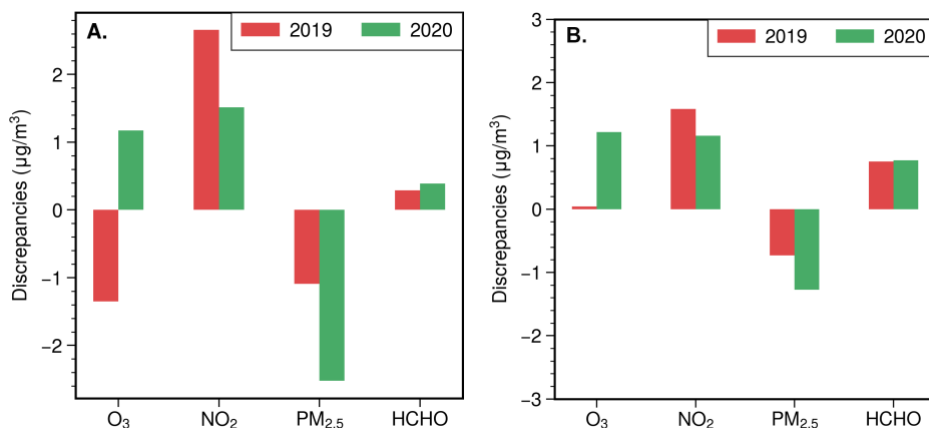
405

406   **Figure 5.** The discrepancies of O_3, NO_2, and $PM_{2.5}$ between urban and non-urban from
407   2019 to 2020 for the lockdown period (A) and summertime (B) averaged concentration.
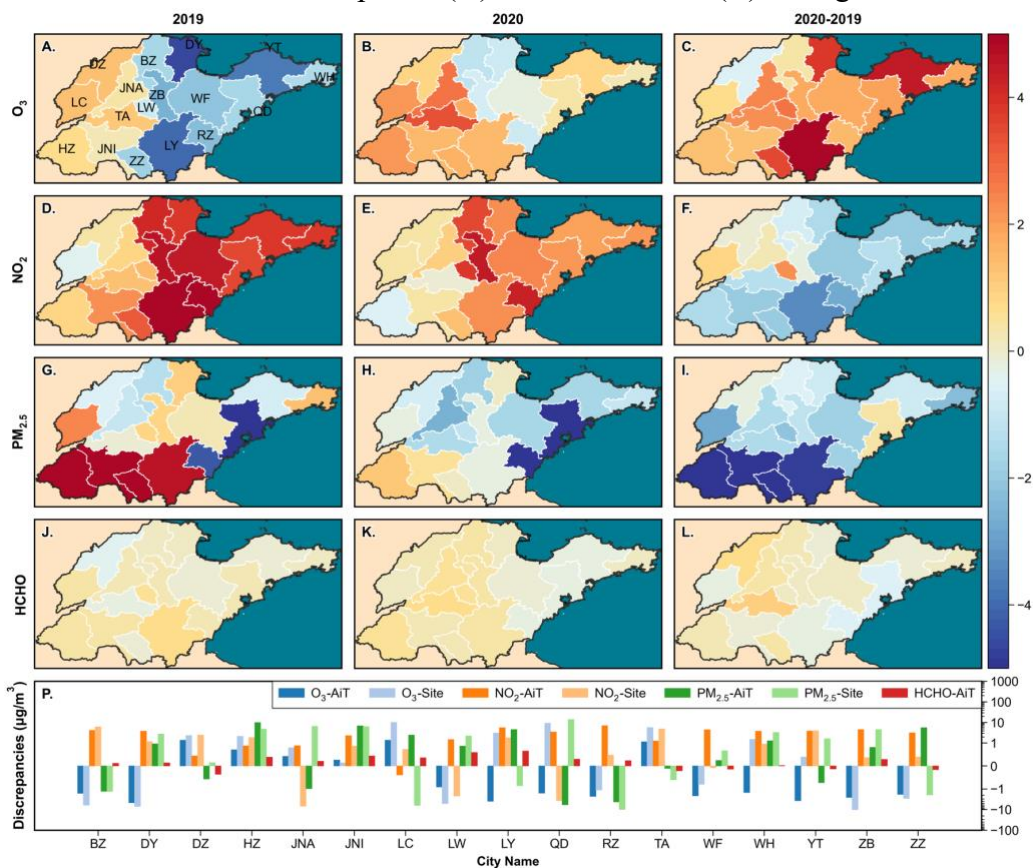
408

409   **Figure 6.** The urban-nonurban disparities of O_3, NO_2, $PM_{2.5}$, and HCHO calculated by
410   AiT across cities with administrative divisions in Shandong, China during lockdown
411   periods in 2019 (A, D, G, J) and 2020 (B, E, H, K), and the changes of differences
412   between 2019 and 2020 (C, F, I, L). P is the comparison between the results of
413   monitoring station data and the AiT dataset in 2019. The red color represents a greater
414   decline in air pollutants in nonurban areas, while the blue color indicates a more

415 significant reduction in urban areas in the third column of the figure. (YT: Yantai, BZ:

416 Binzhou, DY: Dongying, WH: Weihai, DZ: Dezhou, JNA: Jinan, QD: Qingdao, WF:

417 Weifang, ZB: Zibo, LC: Liaocheng, LW: Laiwu, TA: Taian, LY: Linyi, RZ: Rizhao, JNI:

418 Jining, HZ: Hezhe, ZZ: Zaozhuang)

419 **3.3 Photochemical Regimes**

420 **3.3.1 Ozone-NO_x-VOCs-Aerosols Sensitivity**

421 Figure S15 shows the seasonal maps of O_3, $PM_{2.5}$, and NO_2 estimations from AiT,

422 and satellite-derived surface HCHO. Based on these data, we first capture the well-

423 established non-linearities in O_3-VOC-NO_x chemistry by a conceptual framework

424 similar to classic O_3 isopleths typically generated with models (Pusede et al., 2015; Ren

425 et al., 2022a). **Figure 7**A depicts O_3 concentration as a function of HCHO and NO_2,

426 which was derived solely from ground-level estimation. The result indicates that the O_3

427 regimes can be qualitatively identified based on the nonlinear interaction between

428 surface O_3, HCHO, and NO_2. In the regime characterized by high NO_2 and low HCHO,

429 the elevated consumption of HO_x, predominantly driven by the OH + NO_2 termination

430 reaction, results in the suppression of NO_x on O_3, indicating the prevalence of VOC-

431 limited chemistry. Conversely, when HCHO levels are high and NO_2 levels are

432 relatively low, O_3 increases with NO_2 and exhibits insensitivity to HCHO due to

433 abundant peroxyl radicals (HO_2 + organic peroxy (RO_2) radicals, RO_x) self-reactions,

434 suggesting NO_x-limited (VOC-saturated) chemistry. In cases where high HCHO and

435 NO_2, the O_3 increases with both HCHO and NO_2, reaching a peak. While **Figure 7**A

436 resembles this overall O_3-VOC-NO_x, the blurry transition between two different

437 regimes and the role of $PM_{2.5}$ is uncertain which may be influenced by meteorological

438   conditions, chemical and depositional loss of O_3, errors of estimations, and "aerosol-

439   inhibited". Increasing $PM_{2.5}$ levels could suppress O_3 formation even under high HCHO

440   and NO_2 conditions (**Figure 7**B), which could be induced by enhanced reactive uptake

441   of HO_2 onto aerosol particles and weaker photochemical reaction resulting from the

442   scattering and absorption of solar radiation by anthropogenic aerosols. The relationship

443   between $PM_{2.5}$ and O_3 in Shandong demonstrates the distinct stages of O_3 chemistry, as

444   depicted in **Figure 7**C. When $PM_{2.5}$ was below the maximum turning point (MTP1, 35

445    $\mu g/m^3$), a linear and positive correlation between O_3 and $PM_{2.5}$ was observed due to the

446   common dependence on precursors in the initial stage (Zhang et al., 2022). As $PM_{2.5}$

447   increased beyond the MTP1, a sharp reduction in HCHO and O_3 was observed,

448   accompanied by a decline in surface short-wave radiation, reflecting their formation as

449   photo-oxidation products of OVOCs and NO_x. When $PM_{2.5}$ exceeded the minimum

450   transition point (MTP2, 45 $\mu g/m^3$), a phase was observed with stagnant radiation

451   intensity and relatively higher NO_2 levels compared to HCHO. This regime is typically

452   associated with a VOC-limited regime, where an increase in HCHO and a decrease in

453   NO_2 concentration could promote O_3 production. However, our findings demonstrated

454   an opposite impact of HCHO and NO_2 on O_3 when $PM_{2.5}$ exceeded MTP2. **Figure 7**D

455   shows the changes in the quantitative relationships between $HCHO/NO_2$ (FNR) and O_3

456   by artificially changing $PM_{2.5}$ and precursors levels for XGBoost, in which the peak of

457   curves marks the transitional threshold of O_3 regimes from VOC to NO_x sensitive. It

458   can be seen that attenuated $PM_{2.5}$ pollution could increase the sensitivity of O_3 to VOCs

459 and decrease the sensitivity to NO_x, which causes the shift in O_3 regimes from NO_x-

460 limited to VOC-limited. With the recent reduction in NO_x emissions in China, the

461 anticipated transition of the O_3 production regime in urban areas towards being more

462 NO_x-limited has been impeded by the heightened VOC sensitivity resulting from

463 decreased $PM_{2.5}$ levels. Our results are consistent with the findings of Li et al. regrading

464 O_x-NO_x relationship in response to changing $PM_{2.5}$ (Li et al., 2022a), and with the

465 findings of Dyson et al. on the impact of HO_2 aerosol uptake on O_3 production (Dyson

466 et al., 2023). The SHAP interaction plots in **Figures 7**E and F illustrate that the

467 influence of NO_2 and HCHO on O_3 formation is not constant and is influenced by the

468 levels of $PM_{2.5}$. Typically, at a certain level of $PM_{2.5}$, a lower NO concentration results

469 in a stronger inhibitory effect on O_3 production. This could be due to aerosols exerting

470 stronger suppression through the HO_2 sink at lower NO_x levels. As the concentration of

471 $PM_{2.5}$ increases, often accompanied by a concurrent increase in NO_2 as a key precursor,

472 there is a greater need for higher levels of NO_2 to be converted into nitrous acid (HONO)

473 through the heterogeneous uptake by aerosols. This process produces more OH radicals,

474 which facilitate photochemical O_3 formation, thereby offsetting the increased inhibitory

475 effect of the HO_2 sink. Under high $PM_{2.5}$ concentrations, an increase in NO_2 along with

476 a decrease in HCHO enhances their effect on promoting O_3 formation. This

477 enhancement could be caused by increased titration of O_3 by NO, resulting from weaker

478 conversion of NO to NO_x through the RO_x radical. Meanwhile, the impact of HCHO

479 shifts from promoting to suppressing as $PM_{2.5}$ pollution intensifies. It further illustrates

480   that the scavenging of HO$_2$ on aerosols can cause the shift in O$_3$ regimes from being

481   VOC-limited to NO$_x$-limited and the threshold approach is restricted by aerosols and

482   meteorology for determining the constantly changing O$_3$ formation regimes over time

483   and space.

484
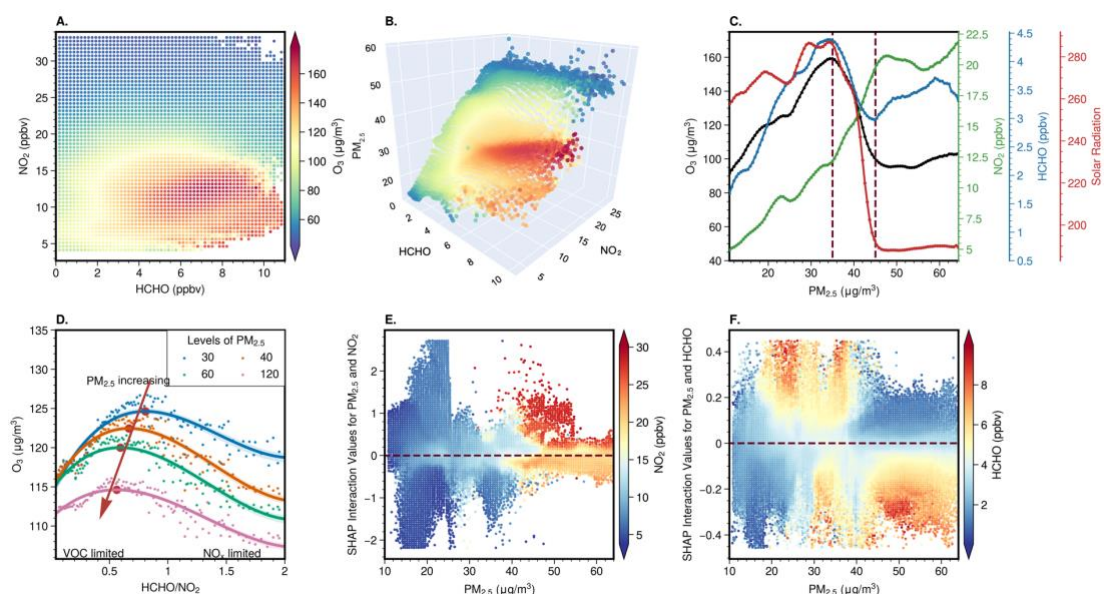
485   **Figure 7.** (A) O$_3$ concentrations as a function of surface HCHO and NO$_2$. (B) O$_3$

486   concentrations as a function of surface HCHO, NO$_2$, and PM$_{2.5}$. Both A and B utilize a

487   shared color bar to indicate O$_3$ concentrations, enhancing comparability. (C)

488   Relationship between O$_3$, and NO$_2$, HCHO, and surface short-wave radiation flux. The

489   paired O$_3$, HCHO, NO$_2$, and solar radiation are divided into 100 bins based on PM$_{2.5}$

490   and then the averaged concentrations (y-axis) are calculated for each PM$_{2.5}$ bin (x-axis).

491   (D) Changes in HCHO/NO$_2$-O$_3$ relationship in response to changing PM$_{2.5}$ by XGBoost

492   model. The solid lines are fitted with four-order polynomial curves, and the shading

493   indicates 95% confidence intervals. (E-F) The interaction SHAP values reveal an

494   interesting hidden relationship between pairwise variables (PM$_{2.5}$ and NO$_2$, HCHO) and

495   O$_3$.

496   Unraveling the intricate interplay of O$_3$ with meteorology, aerosols, and precursors

497   that govern O$_3$ formation over extensive spatial domains has long confounded robust

498   interpretation. These multiscale processes were elucidated using an interpretable ML

499   model, which can quantify the positive or negative contributions of individual processes.

As depicted in Figure S16, the performance of the XGBoost model is robust, evidenced by a high R^2 value of 0.99 coupled with a low RMSE of 3.24 $\mu g/m^3$ and MAE of 2.33 $\mu g/m^3$. Figure S17 elucidates that meteorological variations, chiefly surface short-wave radiation flux modulating photochemical reaction kinetics, primarily dictate the heterogeneous geographic distribution of O_3 at the regional scale, with lower levels over the Jiaodong Peninsula. Meanwhile, local atmospheric chemical processes predominate the city-scale variability of O_3. HCHO facilitated O_3 formation in urban areas yet suppressed it in rural regions across areas with high ozone, where most NO_2 promoted O_3 production overall, indicating VOC-NO_x synergistic control on O_3 in cities and a NO_x-limited regime in rural areas during summertime. The contribution of NO_2 and $PM_{2.5}$ exhibits analogous seasonal variability, promoting O_3 formation under low pollution conditions while inhibiting O_3 when pollution levels are high (Figures S15 and 18). The elevated NO_2 levels in autumn led to a negative contribution to O_3, whereas the facilitating effect of $PM_{2.5}$ was enhanced. This stems from the relatively moderate $PM_{2.5}$ concentrations slightly affecting photochemical reaction rates, while the increased NO_2 amplified the reactive uptake of NO_2 by $PM_{2.5}$, generating more OH radicals that promote O_3 formation (Lin et al., 2023; Tan et al., 2022). In winter, $PM_{2.5}$ pollution exceeding 75 $\mu g/m^3$ suppressed O_3 formation through scattering and absorbing solar radiation that activates atmospheric chemical processes, which counteracted the promoting effect of high $PM_{2.5}$ through the conversion of NO_2 to HONO.

521
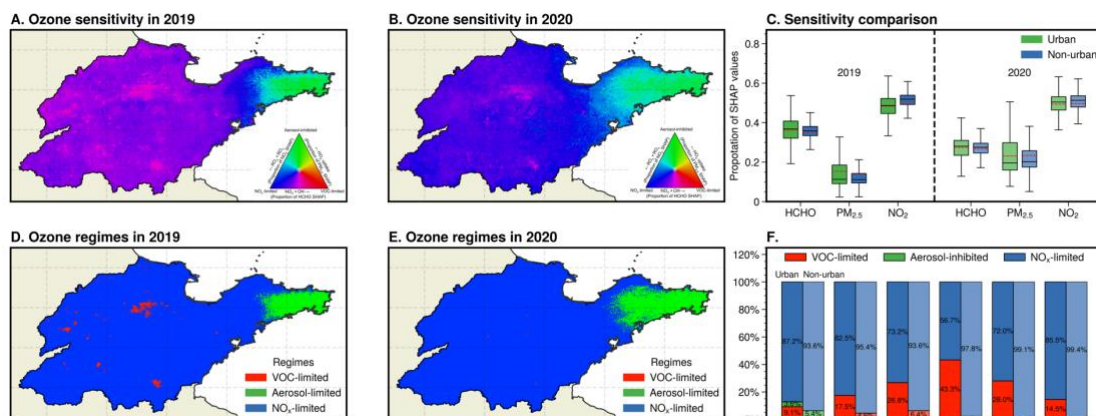
Figure 8. Comparison of geographical distribution for ozone formation regimes between 2019 and 2020 in the summertime. All surface daily O_3, $PM_{2.5}$, and NO_2 estimations from Air Transformer (AiT) are averaged over each month from May to October 2019-2020 for matching monthly HCHO derived from TROPOMI (500 * 500 m). (A, B) Geographical distribution of fractional contribution of chemical factors representing O_3 formation regimes. The ternary phase diagram in the legend depicts the normalized fraction of SHAP values for O_3 attributed to HCHO, NO_2, and $PM_{2.5}$ at the surface, representing VOC-limited (red), aerosol-inhibited (green), and NO_x-limited (blue) regimes, respectively. (C) Statistical Changes in the fractional contribution of chemical factors. (D, E) Geographical distribution of O_3 chemical regimes. (F) Proportion of three O_3 chemical regimes across urban and nonurban areas in 2019 in Shandong (SD), and individual cities (BZ: Binzhou, ZB: Zibo, LC: Liaocheng, LY: Linyi, JNI: Jining).

Figure 8A-C shows surface distribution and changes of the relative proportions of

SHAP values on three pollutants for inferring O_3 photochemical regimes. Moving along

an urban-to-rural gradient, reactions dominated by RO_x radical self-reactions are

continuously enhanced with increasing NO_x SHAP values, resulting in the majority of

rural Shandong being situated in NO_x-limited regimes. Furthermore, the overall ozone

production regimes in Shandong exhibited a transition toward more NO_x-limited from

2019 to 2020, with regions dominated by NO_x-limited shifting toward being aerosol-

inhibited in the Jiaodong Peninsula. The aerosol-inhibited regime differs from either of

543   the two classically applied tropospheric O_3 policy-control regimes. It is attributed to the

544   predominant heterogeneous HO_2 uptake by aqueous aerosols, despite comparatively

545   low $PM_{2.5}$ levels during summertime. The marine environment engenders liquid aerosol

546   particles with HO_2 uptake coefficients exceeding those of dry aerosols by orders of

547   magnitude (Song et al., 2022a). Concurrently, lower ambient NO_x levels minimize the

548   promotive effects of aerosols on ozone formation (Tan et al., 2022; Kohno et al., 2022).

549   This result is consistent with the findings of Dyson et al. (Dyson et al., 2023), which

550   concluded that the contribution of HO_2 sinks onto aerosols on total HO_2 could increase

551   for areas with low NO levels. The attenuated responsiveness of O_3 formation to VOCs

552   induced by the uptake of HO_2 results in enhanced sensitivity of NO_x at the northwest

553   boundary region of the Jiaodong Peninsula. Collectively, these processes delineate an

554   aerosol-inhibited ozone production regime in this coastal region, reflecting the

555   sensitivity of O_3 photochemistry to the HO_2 sink. In several cities, including Binzhou,

556   Zibo, Liaocheng, Linyi, and Jining, a greater proportion of urban areas, as compared to

557   their nonurban counterparts, exhibited a VOC-limited regime in 2019, as indicated by

558   the prevalence of red regions in **Figure 8**D. The percentage of urban areas in these cities

559   under a VOC-limited regime ranges from 15% to 43%, in stark contrast to non-urban

560   areas where such a regime is typically rare (**Figure 8**F). The comparison of O_3

561   sensitivities from 2019 to 2020 shows a regional shift towards increased sensitivity to

562   aerosol and NO_x, along with a decreased VOC sensitivity as a result of NO_x reduction

563   (**Figure 8**A-C). This shift has led to the majority of areas in Shandong being dominated

564   by a NO$_x$-limited regime in 2020, with an expanded aerosol-inhibited regime region in

565   the Jiaodong Peninsula (**Figure 8**E). Additionally, the discrepancy in O$_3$ formation

566   sensitivity between urban and non-urban areas has been diminishing during this period

567   (**Figure 8**C). As illustrated in **Figure 9**, while the ozone regime transitions towards

568   NO$_x$-limited, there is a marked shift towards greater aerosol sensitivity across nearly

569   90% of areas, leading to a 1.6% increase in aerosol-inhibited grids. Compared to

570   nonurban regions, a higher number of grids in urban areas demonstrate a shift towards

571   NO$_x$ sensitivity. Conversely, urban areas that were predominantly aerosol-inhibited in

572   2019 showed a lower sensitivity shift towards NO$_x$.
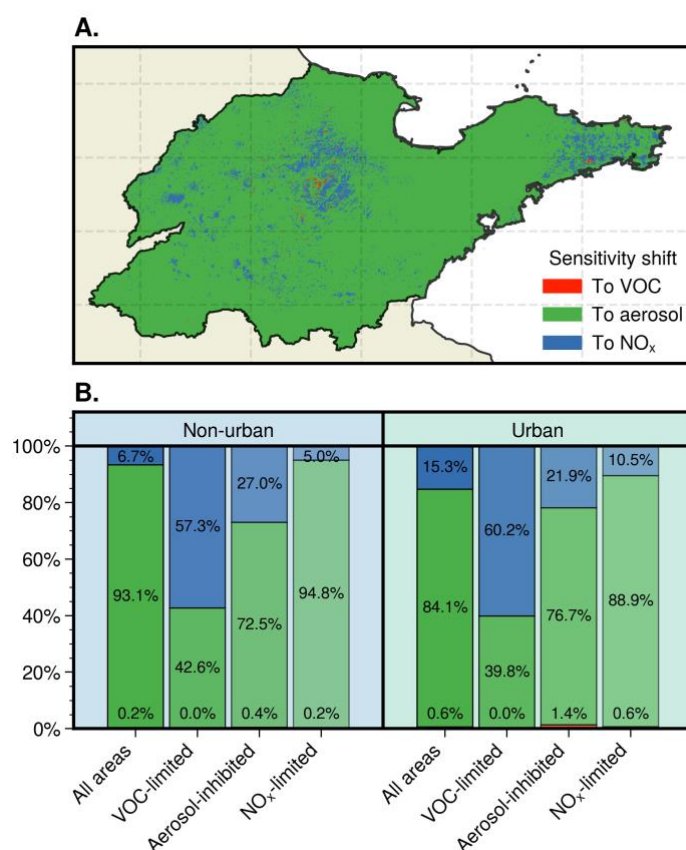
573

574   **Figure 9.** Geographical distribution of changes in ozone sensitivity from 2019 to 2020
575   in summertime (A). Comparison of ozone sensitivity changes across areas dominated
576   by different chemical regimes in 2019 between urban and non-urban areas (B).

3.3.2 Impact on Urban-nonurban Differences

577

578   We further explore the reversed O_3 differences by separating the individual

579 contributions of climate and anthropogenic changes using an interpretable machine

580 learning model (**Figure 10**). The results demonstrate that atmospheric chemical

581 processes and meteorological conditions commonly dominate the discrepancies in O_3

582 levels between urban and non-urban areas. From 2019 to 2020, meteorological shifts

583 remained uniform across urban and non-urban regions, marked by lowered surface

584 pressure, boundary layer height, and short-wave radiation, alongside heightened

585 precipitation. This, coupled with decreased precursor levels, contributed to a decline in

586 O_3 pollution. As shown in **Figures 10** and S19, the diminished reduction in boundary

587 layer height and radiation flux across urban areas, compared to nonurban areas in 2020,

588 decelerated the expected decline of O_3 concentrations, leading to urban O_3 levels

589 exceeding those of nonurban areas. Concurrently, a narrowing difference in

590 temperatures between urban and nonurban areas, despite an overall cooling from 2019

591 to 2020, favored O_3 formation in urban regions during the summertime. Additionally,

592 $PM_{2.5}$ emerged as the principal anthropogenic factor inverting the urban-nonurban O_3

593 disparity over the course of 2019 to 2020. Its contribution to ozone shifted from being

594 lower in urban areas to exceeding that in nonurban areas, revealing that the decreased

595 reactive uptake of HO_2 from aerosols induced by a more substantial reduction in $PM_{2.5}$

596 in urban areas made the larger contribution to O_3 production (Ivatt et al., 2022; Li et al.,

597 2017). Moreover, the response of O_3 to the changes in its precursors and $PM_{2.5}$ was

598   determined by the O_3 formation regimes. The variations in O_3 sensitivity also

599   corroborate the above finding. In rural areas, where there was a lesser reduction in $PM_{2.5}$

600   concentration, the sensitivity increasingly favored aerosol suppression across more than

601   93% of the assessed grids (**Figure 9**). This enhanced suppression effect of aerosols in

602   rural areas leads to a more significant O_3 reduction compared to urban locales. The

603   reduction of NO_x in nonurban areas demonstrated a more effective reduction in O_3

604   levels, which predominantly shifted towards a NO_x-limited regime in 2020. Although

605   urban areas also showed a shift towards being a NO_x-limited regime, they exhibited

606   relatively higher sensitivity to VOCs (**Figure 8**). The urban areas, characterized by

607   elevated NO_x emissions, exhibited a higher sensitivity to VOCs, and the fraction of

608   aerosol-inhibited areas increased from 2019 to 2020, resulting in the control benefits of

609   urban O_3 pollution in 2020 are partially offset by the nonlinear response of O_3 to a

610   greater reduction in NO_2 and $PM_{2.5}$, and a smaller decrease in HCHO relative to

611   nonurban areas. Consequently, O_3 exhibits a lower reduction in urban areas as a result

612   of the aforementioned changes.

613
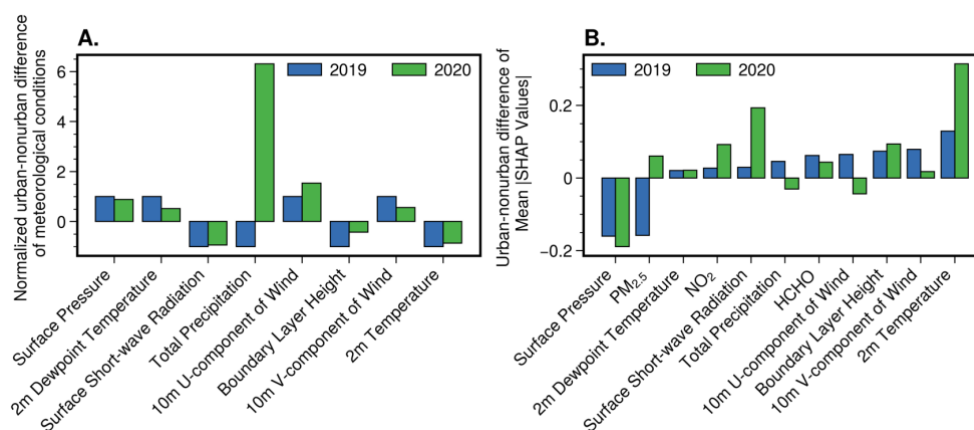
Figure 10. Comparison of urban-nonurban disparities in meteorological conditions (A), and mean absolute SHAP values (B) between 2019 and 2020 across Shandong, China during the summertime.

4. CONCLUSIONS

The purpose of the current study was to diagnose the non-linearity of O_3-NO_x-VOCs-aerosols chemistry using an interpretable ML model based on spatially resolved multi-pollutant estimations for determining the causes of changing differences in O_3 levels between urban and non-urban areas. Our study represents the first attempt to develop an advanced DL model that reconstructs the concentrations of multiple pollutants and subsequently infers the aerosol-inhibited regime from observations. This innovative approach provides further support for investigating the impact of precursor emissions and aerosol on the urban-nonurban differences in O_3 levels.

Given the non-linearity of ozone formation and its increasing regional differences, precise estimations of ground-level O_3, NO_2, HCHO, and $PM_{2.5}$ are crucial for deducing the chemical regimes governing ozone pollution and its urban-nonurban disparities. The evaluation of the model's performance indicates that it can be readily extended to any other domain thanks to its unified architecture. Anyone can easily utilize the model to estimate ground-level pollutants, intelligently considering spatial-temporal neighborhood information based on their customized input data. The model further improved spatial resolution to sub-km levels using TROPOMI and MODIS retrievals via spatiotemporal autocorrelation downscaling of AiT. The "black box" nature of AiT can be made more physically interpretable by SHAP, enabling the evaluation of the

636   significance of each input variable (Figure S20). The season trends show the highest

637   contribution, followed by emission proxies and meteorological conditions. Meanwhile,

638   the results between AiT trained with all data and that trained exclusively with CNEMC

639   data across various spatiotemporal scales underscore the promising prospect for

640   improving the model's generalization ability with more ground-level monitoring data

641   and the growing space of methods.

642   We conclude that with the effective reduction of $PM_{2.5}$ pollution, the sensitivity of

643   O_3 to VOCs will increase, necessitating further intensification of VOC emissions

644   regulation by government agencies. Three distinct chemical regimes were assessed by

645   tracking NO_x, VOCs, and aerosols with surface NO_2, HCHO, and $PM_{2.5}$. In the

646   Jiaodong Peninsula of Shandong Province, coastal areas with relatively few primary

647   pollutants are widely found to be under an aerosol suppression regime, illustrating that

648   ozone regime inference based on machine learning can serve as an alternative to

649   determining the aerosol suppression regime through the rate of radical termination in

650   atmospheric chemical models. The O_3 regime in other areas of Shandong generally

651   transited from the NO_x-sensitive regime in nonurban to a more VOC-sensitive regime

652   in urban areas. We estimate that substantial reductions in anthropogenic emissions of

653    $PM_{2.5}$ and NO_2 are the main drivers of the reversal of the traditional discrepancy in O_3

654   levels between urban and non-urban areas. In essence, due to the lower efforts in

655   reducing $PM_{2.5}$ in nonurban settings, the aerosol-mediated suppression of ozone

656   became more pronounced, resulting in lower ozone levels in rural areas relative to urban

657   centers. This shift underlines the intricate balance between emission reduction and

658   ozone formation mechanisms, suggesting that nuanced understanding and targeted

659   interventions are necessary to manage and mitigate the health and environmental

660   impacts of such disparities. To preclude exacerbated O_3 pollution resulting from the

661   shift of many regions from VOC-limited to NO_x-limited regimes and the decline in

662   heterogeneous HO_2 uptake induced by $PM_{2.5}$ reduction in urban areas, emission policies

663   aimed at decreasing NO_x to reduce O_3 levels will only be effective with stringent VOC

664   emission abatement when $PM_{2.5}$ is concurrently decreased. The integration of high-

665   resolution pollutant estimations with an interpretable machine learning model offers a

666   promising avenue for advancing our understanding of ozone pollution dynamics and

667   developing effective air quality management strategies.

668   Although our study endeavors to establish O_3 formation regimes involving NO_x,

669   VOCs, and aerosols, and the method identifies an aerosol-inhibited regime from a

670   statistical perspective, it is subject to certain uncertainties due to the relatively poor data

671   quality of HCHO and the unsegregated multiple impacts of aerosols, such as N_2O_5

672   uptake, NO_2 uptake, HO_2 uptake, and light extinction (Tan et al., 2022). We have made

673   efforts to integrate all required surface pollutant concentrations into a unified model,

674   while the absence of ground-level HCHO monitoring data compelled us to tap into an

675   alternative methodology. The retrieval error of surface HCHO and the system error

676   between its retrieval approach and the AiT model degrade the ability of ML to identify

677   the O_3 sensitivity. Meanwhile, the notion of ozone regimes is only appreciated in

678   photochemically active environments where the RO_x-HO_x cycle is active (Souri et al.,

679   2023). The definition of NO_x-limited or VOC-limited regimes is meaningless in

680   nighttime chemistry, where NO-O_3-NO_2 partitioning is the primary driver. The surface

681   daytime pollutant estimations with finer resolutions in space and time based on a unified

682   modeling framework will offer an unprecedented view to characterize the near-surface

683   O_3 formation regimes. Notwithstanding the relatively limited duration of the study, this

684   work offers valuable insights into the current state and causes of urban-nonurban

685   disparities in O_3 pollution. Future efforts should conduct a more detailed long-term

686   evaluation of urban-nonurban disparities in global O_3 levels and the impact of formation

687   mechanisms to further our understanding of air pollution and its mitigation.

688 **Competing Interests**

689   The authors declare that they have no conflict of interest.

690 **Acknowledgments**

691   The work was financially supported by the National Natural Science Foundation

692   of China (project No. 22236004) and Taishan Scholars (No. ts201712003).

693 **Code and Data Availability**

694   The Air Transformer deep learning framework is available on GitHub

695   (https://github.com/myles-tcl/Air-Transformer), which provides the scripts for

696   spatiotemporal data extraction, normalization, model training, and estimating of multi-

697   pollutants. The sources of input data in the Air Transformer can be found in Table S1.

698   The estimation of the Air Transformer can be downloaded from Zenodo:

699   https://zenodo.org/records/10071408 (Tao, 2023).

Author Contributions

701   CT: Methodology, Software, Validation, Formal analysis, Investigation, Data

702   Curation, Writing-Original Draft, Visualization. YP: Conceptualization, Writing-

703   Review & Editing. QZ: Writing-Review & Editing, Project administration, Funding

704   acquisition. YZ: Methodology, Writing-Review & Editing. BG: Software, Writing-

705   Review & Editing. QW: Supervision, Writing-Review & Editing. WW: Supervision,

706   Writing-Review & Editing.

707

References

Bertasius, G., Wang, H., and Torresani, L.: Is Space-Time Attention All You Need for Video Understanding?, http://arxiv.org/abs/2102.05095, 9 June 2021.

Chen, T. and Guestrin, C.: XGBoost: A Scalable Tree Boosting System, in: Proceedings of the 22nd ACM SIGKDD International Conference on Knowledge Discovery and Data Mining, KDD'16: The 22nd ACM SIGKDD International Conference on Knowledge Discovery and Data Mining, San Francisco California USA, 785–794, https://doi.org/10/gdp84q, 2016.

Action Plan on Air Pollution Prevention and Control (in Chinese): http://www.gov.cn/zwgk/2013-09/12/content_2486773.htm, last access: 1 February 2023.

Chu, W., Li, H., Ji, Y., Zhang, X., Xue, L., Gao, J., and An, C.: Research on ozone formation sensitivity based on observational methods: Development history, methodology, and application and prospects in China, Journal of Environmental Sciences, S1001074223000980, https://doi.org/10/gr4qzk, 2023.

Cooper, M. J., Martin, R. V., Hammer, M. S., Levelt, P. F., Veefkind, P., Lamsal, L. N., Krotkov, N. A., Brook, J. R., and McLinden, C. A.: Global fine-scale changes in ambient NO_2 during COVID-19 lockdowns, Nature, 601, 380–387, https://doi.org/10.1038/s41586-021-04229-0, 2022.

Copernicus Sentinel-5P (processed by ESA): TROPOMI Level 2 Ozone Total Column products (Version 02), https://doi.org/10.5270/S5P-ft13p57, 2020.

Di, Q., Kloog, I., Koutrakis, P., Lyapustin, A., Wang, Y., and Schwartz, J.: Assessing $PM_{2.5}$ Exposures with High Spatiotemporal Resolution across the Continental United States, Environ. Sci. Technol., 50, 4712–4721, https://doi.org/10.1021/acs.est.5b06121, 2016.

Dias, D. and Tchepel, O.: Spatial and Temporal Dynamics in Air Pollution Exposure Assessment, IJERPH, 15, 558, https://doi.org/10.3390/ijerph15030558, 2018.

Didan, K.: MODIS/Terra Vegetation Indices 16-Day L3 Global 250m SIN Grid V061,

736 NASA EOSDIS Land Processes Distributed Active Archive Center,

737 https://doi.org/10.5067/MODIS/MOD13Q1.061, 2021.

738 van Donkelaar, A., Martin, R. V., Spurr, R. J. D., and Burnett, R. T.: High-Resolution

739 Satellite-Derived $PM_{2.5}$ from Optimal Estimation and Geographically Weighted

740 Regression over North America, Environ. Sci. Technol., 49, 10482–10491,

741 https://doi.org/10.1021/acs.est.5b02076, 2015.

742 Dosovitskiy, A., Beyer, L., Kolesnikov, A., Weissenborn, D., Zhai, X., Unterthiner, T.,

743 Dehghani, M., Minderer, M., Heigold, G., Gelly, S., Uszkoreit, J., and Houlsby,

744 N.: An Image is Worth 16x16 Words: Transformers for Image Recognition at Scale,

745 https://doi.org/10.48550/arXiv.2010.11929, 3 June 2021.

746 Dyson, J. E., Whalley, L. K., Slater, E. J., Woodward-Massey, R., Ye, C., Lee, J. D.,

747 Squires, F., Hopkins, J. R., Dunmore, R. E., Shaw, M., Hamilton, J. F., Lewis, A.

748 C., Worrall, S. D., Bacak, A., Mehra, A., Bannan, T. J., Coe, H., Percival, C. J.,

749 Ouyang, B., Hewitt, C. N., Jones, R. L., Crilley, L. R., Kramer, L. J., Acton, W. J.

750 F., Bloss, W. J., Saksakulkrai, S., Xu, J., Shi, Z., Harrison, R. M., Kotthaus, S.,

751 Grimmond, S., Sun, Y., Xu, W., Yue, S., Wei, L., Fu, P., Wang, X., Arnold, S. R.,

752 and Heard, D. E.: Impact of HO_2 aerosol uptake on radical levels and O_3

753 production during summertime in Beijing, Atmos. Chem. Phys., 23, 5679–5697,

754 https://doi.org/10/gshrst, 2023.

755 Geng, G., Xiao, Q., Liu, S., Liu, X., Cheng, J., Zheng, Y., Xue, T., Tong, D., Zheng, B.,

756 Peng, Y., Huang, X., He, K., and Zhang, Q.: Tracking Air Pollution in China: Near

757 Real-Time $PM_{2.5}$ Retrievals from Multisource Data Fusion, Environ. Sci. Technol.,

758 55, 12106–12115, https://doi.org/10.1021/acs.est.1c01863, 2021.

759 Global Modeling and Assimilation Office (GMAO): MERRA-2 inst3_2d_gas_Nx: 2d,

760 3-Hourly, Instantaneous, Single-Level, Assimilation, Aerosol Optical Depth

761 Analysis V5.12.4, Greenbelt, MD, USA, Goddard Earth Sciences Data and

762 Information Services Center (GES DISC),

763 https://doi.org/10.5067/HNGA0EWW0R09, 2015.

764 Han, H., Zhang, L., Liu, Z., Yue, X., Shu, L., Wang, X., and Zhang, Y.: Narrowing
765   Differences in Urban and Nonurban Surface Ozone in the Northern Hemisphere
766   Over 1990–2020, Environ. Sci. Technol. Lett., 10, 410–417,
767   https://doi.org/10/gsd5gk, 2023.

768 Han, X. and Naeher, L. P.: A review of traffic-related air pollution exposure assessment
769   studies in the developing world, Environment International, 32, 106–120,
770   https://doi.org/10.1016/j.envint.2005.05.020, 2006.

771 Hersbach, H., Bell, B., Berrisford, G., Horányi, A., Muñoz Sabater, J., Nicolas, J.,
772   Peubey, C., Rozum, I., Schepers, D., Simmons, A., Soci, C., Dee, D., and Thépaut,
773   J.-N.: ERA5 hourly data on single levels from 1959 to present, Copernicus Climate
774   Change Service (C3S) Climate Data Store (CDS),
775   https://doi.org/10.24381/cds.adbb2d47, 2023.

776 Huang, C., Hu, J., Xue, T., Xu, H., and Wang, M.: High-Resolution Spatiotemporal
777   Modeling for Ambient $PM_{2.5}$ Exposure Assessment in China from 2013 to 2019,
778   Environ. Sci. Technol., 55, 2152–2162, https://doi.org/10.1021/acs.est.0c05815,
779   2021.

780 Inness, A., Ades, M., Agustí-Panareda, A., Barré, J., Benedictow, A., Blechschmidt, A.-
781   M., Dominguez, J. J., Engelen, R., Eskes, H., Flemming, J., Huijnen, V., Jones, L.,
782   Kipling, Z., Massart, S., Parrington, M., Peuch, V.-H., Razinger, M., Remy, S.,
783   Schulz, M., and Suttie, M.: The CAMS reanalysis of atmospheric composition,
784   Atmos. Chem. Phys., 19, 3515–3556, https://doi.org/10/ghdkrm, 2019.

785 Ivatt, P. D., Evans, M. J., and Lewis, A. C.: Suppression of surface ozone by an aerosol-
786   inhibited photochemical ozone regime, Nat. Geosci., 15, 536–540,
787   https://doi.org/10.1038/s41561-022-00972-9, 2022.

788 Jerrett, M., Arain, A., Kanaroglou, P., Beckerman, B., Potoglou, D., Sahsuvaroglu, T.,
789   Morrison, J., and Giovis, C.: A review and evaluation of intraurban air pollution
790   exposure models, Journal of Exposure Science & Environmental Epidemiology,
791   15, 185–204, https://doi.org/10.1038/sj.jea.7500388, 2005.

Jin, X., Fiore, A. M., Murray, L. T., Valin, L. C., Lamsal, L. N., Duncan, B., Folkert Boersma, K., De Smedt, I., Abad, G. G., Chance, K., and Tonnesen, G. S.: Evaluating a Space-Based Indicator of Surface Ozone-NO$_x$-VOC Sensitivity Over Midlatitude Source Regions and Application to Decadal Trends: Space-Based Indicator of O$_3$ Sensitivity, J. Geophys. Res. Atmos., 122, 10,439-10,461, https://doi.org/10.1002/2017JD026720, 2017.

Jin, X., Fiore, A., Boersma, K. F., Smedt, I. D., and Valin, L.: Inferring Changes in Summertime Surface Ozone-NO$_x$-VOC Chemistry over U.S. Urban Areas from Two Decades of Satellite and Ground-Based Observations, Environ. Sci. Technol., 54, 6518–6529, https://doi.org/10.1021/acs.est.9b07785, 2020.

Jin, X., Fiore, A. M., and Cohen, R. C.: Space-Based Observations of Ozone Precursors within California Wildfire Plumes and the Impacts on Ozone-NO$_x$-VOC Chemistry, Environ. Sci. Technol., 57, 14648–14660, https://doi.org/10.1021/acs.est.3c04411, 2023.

Jun, C., Ban, Y., and Li, S.: China: Open access to Earth land-cover map, Nature, 514, 434–434, https://doi.org/DOI:10.1038/514434c, 2014.

Jung, J., Choi, Y., Souri, A. H., Mousavinezhad, S., Sayeed, A., and Lee, K.: The Impact of Springtime-Transported Air Pollutants on Local Air Quality With Satellite-Constrained NO$_x$ Emission Adjustments Over East Asia, Journal of Geophysical Research: Atmospheres, 127, e2021JD035251, https://doi.org/10.1029/2021JD035251, 2022.

Ke, G., Meng, Q., Finley, T., Wang, T., Chen, W., Ma, W., Ye, Q., and Liu, T.-Y.: LightGBM: A Highly Efficient Gradient Boosting Decision Tree, in: Proceedings of the 31st International Conference on Neural Information Processing Systems, Red Hook, NY, USA, event-place: Long Beach, California, USA, 3149–3157, 2017.

Kohno, N., Zhou, J., Li, J., Takemura, M., Ono, N., Sadanaga, Y., Nakashima, Y., Sato, K., Kato, S., Sakamoto, Y., and Kajii, Y.: Impacts of missing OH reactivity and

820   aerosol uptake of HO_2 radicals on tropospheric O_3 production during the AQUAS-

821   Kyoto summer campaign in 2018, Atmospheric Environment, 281, 119130,

822   https://doi.org/10/gshfc4, 2022.

823   Lamsal, L. N., Krotkov, N. A., Marchenko, S. V., Joiner, J., Oman, L., Vasilkov, A.,

824   Fisher, B., Qin, W., Yang, E.-S., Fasnacht, Z., Choi, S., Leonard, P., and Haffner,

825   D.: TROPOMI/S5P NO_2 Tropospheric, Stratospheric and Total Columns MINDS

826   1-Orbit L2 Swath 5.5 km x 3.5 km, Goddard Earth Sciences Data and Information

827   Services   Center   (GES   DISC),

828   https://doi.org/10.5067/MEASURES/MINDS/DATA203, 2022.

829   Lee, H. J., Kuwayama, T., and FitzGibbon, M.: Trends of ambient O_3 levels associated

830   with O_3 precursor gases and meteorology in California: Synergies from ground

831   and satellite observations, Remote Sensing of Environment, 284, 113358,

832   https://doi.org/10.1016/j.rse.2022.113358, 2023.

833   Li, C., Zhu, Q., Jin, X., and Cohen, R. C.: Elucidating Contributions of Anthropogenic

834   Volatile Organic Compounds and Particulate Matter to Ozone Trends over China,

835   Environ. Sci. Technol., 56, 12906–12916, https://doi.org/10.1021/acs.est.2c03315,

836   2022a.

837   Li, D., Wang, S., Xue, R., Zhu, J., Zhang, S., Sun, Z., and Zhou, B.: OMI-observed

838   HCHO in Shanghai, China, during 2010–2019 and ozone sensitivity inferred by

839   an improved HCHO / NO_2 ratio, Atmos. Chem. Phys., 21, 15447–15460,

840   https://doi.org/10.5194/acp-21-15447-2021, 2021a.

841   Li, K., Jacob, D. J., Liao, H., Zhu, J., Shah, V., Shen, L., Bates, K. H., Zhang, Q., and

842   Zhai, S.: A two-pollutant strategy for improving ozone and particulate air quality

843   in China, Nat. Geosci., 12, 906–910, https://doi.org/10.1038/s41561-019-0464-x,

844   2019.

845   Li, K., Wang, Y., Peng, G., Song, G., Liu, Y., Li, H., and Qiao, Y.: UniFormer: Unified

846   Transformer   for   Efficient   Spatial-Temporal   Representation   Learning,

847   International Conference on Learning Representations, 2021b.

848 Li, L. and Wu, J.: Spatiotemporal estimation of satellite-borne and ground-level NO_2

849   using full residual deep networks, Remote Sensing of Environment, 254, 112257,

850   https://doi.org/10.1016/j.rse.2020.112257, 2021.

851 Li, M., Wang, T., Xie, M., Zhuang, B., Li, S., Han, Y., and Chen, P.: Impacts of aerosol-

852   radiation feedback on local air quality during a severe haze episode in Nanjing

853   megacity, eastern China, Tellus B: Chemical and Physical Meteorology, 69,

854   1339548, https://doi.org/10/gsfjz3, 2017.

855 Li, M., Yang, Q., Yuan, Q., and Zhu, L.: Estimation of high spatial resolution ground-

856   level ozone concentrations based on Landsat 8 TIR bands with deep forest model,

857   Chemosphere, 301, 134817, https://doi.org/10.1016/j.chemosphere.2022.134817,

858   2022b.

859 Lin, C., Huang, R.-J., Zhong, H., Duan, J., Wang, Z., Huang, W., and Xu, W.:

860   Elucidating ozone and PM $_{2.5}$ pollution in the Fenwei Plain reveals the co-benefits

861   of controlling precursor gas emissions in winter haze, Atmos. Chem. Phys., 23,

862   3595–3607, https://doi.org/10/gsfvs3, 2023.

863 Liu, M., Huang, Y., Ma, Z., Jin, Z., Liu, X., Wang, H., Liu, Y., Wang, J., Jantunen, M.,

864   Bi, J., and Kinney, P. L.: Spatial and temporal trends in the mortality burden of air

865   pollution in China: 2004–2012, Environment International, 98, 75–81,

866   https://doi.org/10.1016/j.envint.2016.10.003, 2017.

867 Liu, X., Shi, X., Lei, Y., and Xue, W.: Path of coordinated control of $PM_{2.5}$ and ozone

868   in China, Chin. Sci. Bull., 67, 2089–2099, https://doi.org/10.1360/TB-2021-0832,

869   2022.

870 Lu, D., Mao, W., Zheng, L., Xiao, W., Zhang, L., and Wei, J.: Ambient $PM_{2.5}$ Estimates

871   and Variations during COVID-19 Pandemic in the Yangtze River Delta Using

872   Machine Learning and Big Data, Remote Sensing, 13, 1423,

873   https://doi.org/10.3390/rs13081423, 2021.

874 Lu, X., Hong, J., Zhang, L., Cooper, O. R., Schultz, M. G., Xu, X., Wang, T., Gao, M.,

875   Zhao, Y., and Zhang, Y.: Severe Surface Ozone Pollution in China: A Global

876   Perspective, Environ. Sci. Technol. Lett., 5, 487–494,

877   https://doi.org/10.1021/acs.estlett.8b00366, 2018.

878   Lundberg, S. M. and Lee, S.-I.: A Unified Approach to Interpreting Model Predictions,

879   in: Proceedings of the 31st International Conference on Neural Information

880   Processing Systems, Red Hook, NY, USA, 2017.

881   Lyapustin, A. and Wang, Y.: MODIS/Terra+Aqua Land Aerosol Optical Depth Daily

882   L2G Global 1km SIN Grid V061, NASA EOSDIS Land Processes DAAC,

883   https://doi.org/10.5067/MODIS/MCD19A2.061, 2022.

884   Miller, D. F., Alkezweeny, A. J., Hales, J. M., and Lee, R. N.: Ozone Formation Related

885   to Power Plant Emissions, Science, 202, 1186–1188, https://doi.org/10/b5kgjr,

886   1978.

887   Mitchell, R., Frank, E., and Holmes, G.: GPUTreeShap: massively parallel exact

888   calculation of SHAP scores for tree ensembles, PeerJ Computer Science, 8,

889   https://doi.org/10.7717/peerj-cs.880, 2020.

890   Myers, S. L.: The Worst Dust Storm in a Decade Shrouds Beijing and Northern China,

891   The New York Times, 15th March, 2021.

892   Pusede, S. E., Steiner, A. L., and Cohen, R. C.: Temperature and Recent Trends in the

893   Chemistry of Continental Surface Ozone, Chem. Rev., 115, 3898–3918,

894   https://doi.org/10.1021/cr5006815, 2015.

895   Ren, J., Guo, F., and Xie, S.: Diagnosing ozone-NO_x-VOC sensitivity and revealing

896   causes of ozone increases in China based on 2013-2021 satellite retrievals, Atmos.

897   Chem. Phys., 22, 15035–15047, https://doi.org/10.5194/acp-22-15035-2022,

898   2022a.

899   Ren, X., Mi, Z., Cai, T., Nolte, C. G., and Georgopoulos, P. G.: Flexible Bayesian

900   Ensemble Machine Learning Framework for Predicting Local Ozone

901   Concentrations, Environ. Sci. Technol., 56, 3871–3883,

902   https://doi.org/10.1021/acs.est.1c04076, 2022b.

903   Requia, W. J., Di, Q., Silvern, R., Kelly, J. T., Koutrakis, P., Mickley, L. J., Sulprizio,

904   M. P., Amini, H., Shi, L., and Schwartz, J.: An Ensemble Learning Approach for

905   Estimating High Spatiotemporal Resolution of Ground-Level Ozone in the

906   Contiguous United States, Environ. Sci. Technol., 54, 11037–11047,

907   https://doi.org/10.1021/acs.est.0c01791, 2020.

908 Román, M. O., Wang, Z., Sun, Q., Kalb, V., Miller, S. D., Molthan, A., Schultz, L., Bell,

909   J., Stokes, E. C., Pandey, B., Seto, K. C., Hall, D., Oda, T., Wolfe, R. E., Lin, G.,

910   Golpayegani, N., Devadiga, S., Davidson, C., Sarkar, S., Praderas, C., Schmaltz,

911   J., Boller, R., Stevens, J., Ramos González, O. M., Padilla, E., Alonso, J., Detrés,

912   Y., Armstrong, R., Miranda, I., Conte, Y., Marrero, N., MacManus, K., Esch, T.,

913   and Masuoka, E. J.: NASA's Black Marble nighttime lights product suite, Remote

914   Sensing of Environment, 210, 113–143, https://doi.org/10/ghqpjh, 2018.

915 Shapley, L. S.: A value for n-person games, in: The Shapley Value: Essays in Honor of

916   Lloyd S. Shapley, edited by: Roth, A. E., Cambridge University Press, Cambridge,

917   31–40, https://doi.org/10.1017/CBO9780511528446.003, 1988.

918 Shrikumar, A., Greenside, P., and Kundaje, A.: Learning Important Features Through

919   Propagating Activation Differences, http://arxiv.org/abs/1704.02685, 12 October

920   2019.

921 Sicard, P., Serra, R., and Rossello, P.: Spatiotemporal trends in ground-level ozone

922   concentrations and metrics in France over the time period 1999–2012,

923   Environmental Research, 149, 122–144,

924   https://doi.org/10.1016/j.envres.2016.05.014, 2016.

925 Sicard, P., De Marco, A., Agathokleous, E., Feng, Z., Xu, X., Paoletti, E., Rodriguez, J.

926   J. D., and Calatayud, V.: Amplified ozone pollution in cities during the COVID-

927   19 lockdown, Science of The Total Environment, 735, 139542,

928   https://doi.org/10/gg5w8h, 2020.

929 Sillman, S.: The use of NO_y, H_2O_2, and HNO_3 as indicators for ozone-NO_x-hydrocarbon

930   sensitivity in urban locations, J. Geophys. Res., 100, 14175,

931   https://doi.org/10.1029/94JD02953, 1995.

932   Song, H., Lu, K., Dong, H., Tan, Z., Chen, S., Zeng, L., and Zhang, Y.: Reduced Aerosol
933   Uptake of Hydroperoxyl Radical May Increase the Sensitivity of Ozone
934   Production to Volatile Organic Compounds, Environ. Sci. Technol. Lett., 9, 22–29,
935   https://doi.org/10/gnqqb9, 2022a.

936   Song, K., Liu, R., Wang, Y., Liu, T., Wei, L., Wu, Y., Zheng, J., Wang, B., and Liu, S.
937   C.: Observation-based analysis of ozone production sensitivity for two persistent
938   ozone episodes in Guangdong, China, Atmos. Chem. Phys., 22, 8403–8416,
939   https://doi.org/10/gr4qz2, 2022b.

940   Souri, A. H., Johnson, M. S., Wolfe, G. M., Crawford, J. H., Fried, A., Wisthaler, A.,
941   Brune, W. H., Blake, D. R., Weinheimer, A. J., Verhoelst, T., Compernolle, S.,
942   Pinardi, G., Vigouroux, C., Langerock, B., Choi, S., Lamsal, L., Zhu, L., Sun, S.,
943   Cohen, R. C., Min, K.-E., Cho, C., Philip, S., Liu, X., and Chance, K.:
944   Characterization of errors in satellite-based $HCHO/NO_2$ tropospheric column
945   ratios with respect to chemistry, column-to-PBL translation, spatial representation,
946   and retrieval uncertainties, Atmospheric Chemistry and Physics, 23, 1963–1986,
947   https://doi.org/10.5194/acp-23-1963-2023, 2023.

948   Su, W., Hu, Q., Chen, Y., Lin, J., Zhang, C., and Liu, C.: Inferring global surface HCHO
949   concentrations from multisource hyperspectral satellites and their application to
950   HCHO-related global cancer burden estimation, Environment International, 170,
951   107600, https://doi.org/10.1016/j.envint.2022.107600, 2022.

952   Sun, H., Shin, Y. M., Xia, M., Ke, S., Wan, M., Yuan, L., Guo, Y., and Archibald, A. T.:
953   Spatial Resolved Surface Ozone with Urban and Rural Differentiation during
954   1990–2019: A Space–Time Bayesian Neural Network Downscaler, Environ. Sci.
955   Technol., 56, 7337–7349, https://doi.org/10.1021/acs.est.1c04797, 2022.

956   Tan, Z., Lu, K., Ma, X., Chen, S., He, L., Huang, X., Li, X., Lin, X., Tang, M., Yu, D.,
957   Wahner, A., and Zhang, Y.: Multiple Impacts of Aerosols on O_3 Production Are
958   Largely Compensated: A Case Study Shenzhen, China, Environ. Sci. Technol., 56,
959   17569–17580, https://doi.org/10/gsgp79, 2022.

960   Tang, L., Xue, X., Qu, J., Mi, Z., Bo, X., Chang, X., Wang, S., Li, S., Cui, W., and Dong,

961   G.: Air pollution emissions from Chinese power plants based on the continuous

962   emission monitoring systems network, Sci Data, 7, 325, https://doi.org/10/ghfqqf,

963   2020.

964   Tao, C.: Surface Ozone, NO_2, and $PM_{2.5}$ Concentrations Estimated by the Deep

965   Learning model (Air Transformer) based on Satellite data,

966   https://doi.org/10.5281/zenodo.10071408, 2023.

967   Thongthammachart, T., Araki, S., Shimadera, H., Matsuo, T., and Kondo, A.:

968   Incorporating Light Gradient Boosting Machine to land use regression model for

969   estimating NO_2 and $PM_{2.5}$ levels in Kansai region, Japan, Environmental

970   Modelling & Software, 155, 105447,

971   https://doi.org/10.1016/j.envsoft.2022.105447, 2022.

972   Wei, J., Li, Z., Li, K., Dickerson, R. R., Pinker, R. T., Wang, J., Liu, X., Sun, L., Xue,

973   W., and Cribb, M.: Full-coverage mapping and spatiotemporal variations of

974   ground-level ozone (O_3) pollution from 2013 to 2020 across China, Remote

975   Sensing of Environment, 270, 112775, https://doi.org/10.1016/j.rse.2021.112775,

976   2022a.

977   Wei, J., Liu, S., Li, Z., Liu, C., Qin, K., Liu, X., Pinker, R. T., Dickerson, R. R., Lin, J.,

978   Boersma, K. F., Sun, L., Li, R., Xue, W., Cui, Y., Zhang, C., and Wang, J.: Ground-

979   Level NO_2 Surveillance from Space Across China for High Resolution Using

980   Interpretable Spatiotemporally Weighted Artificial Intelligence, Environ. Sci.

981   Technol., acs.est.2c03834, https://doi.org/10.1021/acs.est.2c03834, 2022b.

982   Wei, W., Wang, X., Wang, X., Li, R., Zhou, C., and Cheng, S.: Attenuated sensitivity of

983   ozone to precursors in Beijing–Tianjin–Hebei region with the continuous NOx

984   reduction within 2014–2018, Science of The Total Environment, 813, 152589,

985   https://doi.org/10/gq7ngn, 2022c.

986   WorldPop: Global High Resolution Population Denominators Project - Funded by The

987   Bill and Melinda Gates Foundation (OPP1134076).,

988   https://dx.doi.org/10.5258/SOTON/WP00675, 2018.

989   Xiao, Q., Chang, H. H., Geng, G., and Liu, Y.: An Ensemble Machine-Learning Model

990   To Predict Historical PM$_{2.5}$ Concentrations in China from Satellite Data, Environ.

991   Sci. Technol., 52, 13260–13269, https://doi.org/10.1021/acs.est.8b02917, 2018.

992   Yue, X., Unger, N., Harper, K., Xia, X., Liao, H., Zhu, T., Xiao, J., Feng, Z., and Li, J.:

993   Ozone and haze pollution weakens net primary productivity in China,

994   Atmospheric Chemistry and Physics, 17, 6073–6089, https://doi.org/10.5194/acp-

995   17-6073-2017, 2017.

996   Zhang, J., Wang, J., Sun, Y., Li, J., Ninneman, M., Ye, J., Li, K., Crandall, B., Mao, J.,

997   Xu, W., Schwab, M. J., Li, W., Ge, X., Chen, M., Ying, Q., Zhang, Q., and Schwab,

998   J. J.: Insights from ozone and particulate matter pollution control in New York City

999   applied to Beijing, npj Clim Atmos Sci, 5, 85, https://doi.org/10.1038/s41612-022-

1000   00309-8, 2022.

1001   Zhang, R., Lei, W., Tie, X., and Hess, P.: Industrial emissions cause extreme urban

1002   ozone diurnal variability, Proc. Natl. Acad. Sci. U.S.A., 101, 6346–6350,

1003   https://doi.org/10.1073/pnas.0401484101, 2004.

1004   Zhao, M., Cheng, C., Zhou, Y., Li, X., Shen, S., and Song, C.: A global dataset of annual

1005   urban extents (1992–2020) from harmonized nighttime lights, Earth System

1006   Science Data, 14, 517–534, https://doi.org/10.5194/essd-14-517-2022, 2022.

1007   Zheng, B., Tong, D., Li, M., Liu, F., Hong, C., Geng, G., Li, H., Li, X., Peng, L., Qi, J.,

1008   Yan, L., Zhang, Y., Zhao, H., Zheng, Y., He, K., and Zhang, Q.: Trends in China's

1009   anthropogenic emissions since 2010 as the consequence of clean air actions,

1010   Atmos. Chem. Phys., 18, 14095–14111, https://doi.org/10.5194/acp-18-14095-

1011   2018, 2018.

1012